IX International Conference on Computational Methods in Marine Engineering
MARINE 2021
I.M. Viola and F. Brennan (Eds)

UNDERWATER ACOUSTIC IMPACT OF A MARINE RENEWABLE ENERGY DEVICE

Pedro Pregitzer*, Fernando Lau*, Guilherme Vaz† and Erica Cruz†

*Instituto Superior Técnico (IST)
Universidade de Lisboa
Campus Alameda, Av. Rovisco Pais 1, 1049-001 Lisbon, Portugal

† WavEC Offshore Renewables
Edifício Diogo Cão, Doca de Alcântara Norte, 1350-352 Lisbon, Portugal

Key words: Ocean Acoustics, Underwater Noise Propagation, Verification, Validation

Abstract. Noise generated by renewable energy devices may impact local wildlife and interfere with military navigation techniques. Given the particular challenges posed by underwater sound propagation, careful analysis of this phenomenon is required. To conduct such an analysis, a model that is able to integrate detailed environmental descriptions and low frequency computations is sought. For these purposes, it has been found that normal mode models are the most suited to the task at hand, in particular the classical KRAKEN algorithm. In this article, the advantages of normal mode models over ray-tracing ones such as BELLHOP will be presented. Furthermore, the algorithm's performance is numerically verified through the employment of mesh refinement studies to evaluate its numerical uncertainty convergence characteristics. Finally, the normal mode method's capabilities are validated against experimental data measured near an energy-generating device installed off the coast of Peniche, Portugal. At frequencies above 1000 Hz, it was found that the normal mode solution closely followed the trends observable in the experimental data. Between 500 and 1000 Hz, difficulties in assembling a field solution over the domain arose. Below these frequencies, a clear break-down of the normal mode assumptions was observed. The normal mode method has been concluded to be a strong candidate to predict sound propagation from marine structures, but more work is needed to improve the calculation of near-field effects, potentially by use of Green's function algorithms.

1 INTRODUCTION

Given the ongoing concerns regarding climate change and sustainability, efforts are being focused, throughout all industries, in reducing emissions and negative anthropogenic impacts on the environment and biodiversity. Among these an important area of study is the generation and propagation of noise in the environment [1].

In order to verify compliance with the relevant regulations and reduce environmental impact, several approaches tackling the noise analysis problem can be taken. A straightforward solution would be to conduct experiments characterising the relevant energy device. However, this is a costly and narrow option, valid only for the specific conditions under consideration. A more general approach is to take the numerical route. In this case, one can choose to employ Computational Fluid Dynamics (CFD) to characterise both the noise source and the propagation of sound in the environment, the latter being achieved typically through the Ffowcs Williams-Hawkings (FW-H) analogy[2]. The downside of

this method is its inability to take into account complex acoustic interactions with the environment, such as absorption, as well as assuming range independence for the depth and sound speed profiles. An alternative approach to noise propagation analysis lies in solving the associated wave equation to obtain the resulting noise field, allowing for a more complex description of the environment.

WavEC Offshore Renewables intends to combine the advantages of CFD analysis to characterise a source, making use of the open source ReFRESCO CFD software [3], with propagation algorithms based on the wave equation, to yield a complete noise analysis tool. In this article, the candidate model for the latter component of the framework, KRAKEN[4], will be benchmarked, verified, and validated against experimental data from an offshore wave energy conversion device[5].

KRAKEN[6] is the normal mode component of the Acoustics Toolbox[7], which collects open-source specialised programs for various acoustic problems. Direct access to the source code allow these tools to be fully integrated into the previously mentioned WavEC sound analysis framework, as well as further promoting and developing the open-source spirit of the tool's first component. For verification purposes, the ray-tracing component of the Acoustics Toolbox, known as BELLHOP[8], was used to provide benchmark results, due to its relative simplicity and lower run-times.

The main objectives of this article are to verify and validate KRAKEN, determining the model's numerical convergence conditions and applicability. Verification is achieved by performing multiple mesh refinement studies on benchmark cases[9]. On the other hand, validation of the KRAKEN output is achieved by comparing it to experimental data gathered in the field[5]. If the main objectives are achieved, integration into the WavEC sound analysis framework can begin.

The paper is divided into seven sections, of which this introduction is the first. Section 2 will briefly present the theoretical basis for the wave-based sound propagation algorithms, followed by a description of the numerical implementation of KRAKEN in section 3. In section 4, KRAKEN's performance under various off-ideal conditions is compared to BELLHOP. Section 5 relates to the numerical verification of the algorithm, determining its numerical uncertainty for a given set of meshes. Finally, in section 6 a real-world case is evaluated to validate KRAKEN's results against experimental data, and the paper concludes with section 7.

2 BACKGROUND

2.1 Wave equation

By treating the ocean body as an acoustic medium, the following assumptions are made[4],[10],[11]: the involved Reynolds numbers are high enough that the problem may be considered inviscid; there are no external body forces acting on the medium; the fluid is at rest; all acoustic processes are adiabatic; all variables can be represented as a sum of some constant average value and a variable perturbation component; sources are modelled as points; propagation from source exhibits cylindrical symmetry; and the acoustic field responds in phase with the source.

Gathering all the above assumptions, the final form of the linearised wave equation that serves as the basis for the KRAKEN model reads, in the frequency domain[11]:

$$\frac{1}{\rho_0(z) r}\frac{\partial}{\partial r}\left(r\frac{\partial p(r,z)}{\partial r}\right)+\frac{\partial}{\partial z}\left(\frac{1}{\rho_0(z)}\frac{\partial p(r,z)}{\partial z}\right)-\frac{(i\omega)^2}{\rho_0(z)c^2(z)}p(r,z)=-\frac{1}{\rho_0(z)}\frac{\delta(z-z_s)\delta r}{2\pi r}\,, \qquad (1)$$

where z and r are, respectively, the depth and radial coordinates, ρ_0 is the free-field density, p is the acoustic perturbation pressure, ω represents the angular frequency of oscillation, i is the imaginary unit, and c is the speed of sound in the medium. Moreover, the right-hand side represents a point-source, defined through a Dirac delta function where z_s is the source depth.

2.2 Normal mode solution

The normal mode model of sound propagation takes advantage of the problem's Sturm-Liouville properties[12] to define a set of orthogonal solutions whose sum describes the acoustic pressure field. Assuming the ocean surface and bottom can be described through a set of angle-dependent impedances f^{TOP}, g^{TOP}, f^{BOT} and g^{BOT}, the Helmholtz equation can be written as[4]:

$$p(r,z) = \frac{i}{4\rho_0(z)} \sum_{m=1}^{M} Z_m(z_s) Z_m(z) H_0^{(1)}(k_m r) k_m - \int_{cut} Z_m(z_s) Z_m(z) H_0^{(1)}(k_m r) k_m dk. \,, \tag{2}$$

where M is the total number of propagation modes in depth $Z(z)$, $H_0^{(1)}(k_m r)$ is the Hankel function of the first kind, k represents the eigenvalues of the problem, and coincides with the horizontal wavenumbers, and $\int_{cut}$ represents a branch-cut integral in the complex plane. To obtain the set of the far-field propagation modes Z_m, an ordinary differential equation must be solved, in the form of

$$\rho_0(z) \frac{\partial}{\partial z} \left(\frac{1}{\rho_0(z)} \frac{\partial Z}{\partial z} \right) + \frac{\omega^2}{c^2(z)} Z - k^2 Z = 0 \,, \tag{3}$$

$$f^{TOP}(k^2) Z(0) + \frac{g^{TOP}(k^2)}{\rho_0(0)} \frac{dZ}{dz}(0) = 0 \,, \tag{4}$$

$$f^{BOT}(k^2) Z(D) + \frac{g^{BOT}(k^2)}{\rho_0(D)} \frac{dZ}{dz}(D) = 0 \,, \tag{5}$$

where D is the ocean bottom depth as measured from the ocean surface.

3 IMPLEMENTATION

KRAKEN assumes a constant value for the free-field density ρ_0 within each segment of the given medium. As such, equation (3) can be reduced to a more simple form, and subsequently discretized through finite differences[13]. The vertical point spacing is taken to be constant and described by h, yielding the final set of equations to be computationally solved:

$$\frac{Z_{i+1} - 2Z_i + Z_{i-1}}{h^2} + \left(\frac{\omega^2}{c_i^2} - k^2 \right) Z_i = 0 \,, \tag{6}$$

$$f^{TOP}(k^2) Z_0 + \frac{g^{TOP}(k^2)}{\rho} * \left[\frac{Z_1 - Z_0}{h} + \frac{h}{2} \left(\frac{\omega^2}{c_0^2} - k^2 \right) Z_0 \right] = 0 \,, \tag{7}$$

$$f^{BOT}(k^2) Z_N + \frac{g^{BOT}(k^2)}{\rho} * \left[\frac{Z_N - Z_{N-1}}{h} - \frac{h}{2} \left(\frac{\omega^2}{c_N^2} - k^2 \right) Z_N \right] = 0 \,, \tag{8}$$

where the forward differences approximation was used for the top boundary condition (equation (7)) given the lack of points before the surface $z = z_0$, and the backward differences approximation was used for the bottom boundary condition (equation (8)) at $z = z_N$ for analogous reasons.

For very shallow water and for near-field cases, neglecting the branch-cut integral may give rise to errors propagating into the far-field. As such, KRAKENC, a version of the algorithm computing this term[14] at the cost of increased run-times, is used in this work.

The solution to equations (6)-(8) is obtained for a single source over a vertically uniform mesh optionally determined by the user, which must have at least 10 points per wavelength. In KRAKENC, the system matrix is solved through an eigenvalue deflation method[15], which is a secant-based algorithm. Once the vertical solution is obtained, propagation is determined from the definition of the normal modes and projected onto a grid defined by the user, which has no limitations regarding its

size. The stopping criteria for the iterative solver is based on the maximum range. The final output is a multi-dimensional matrix describing the relative pressure field, normalised to the pressure 1 meter away from the source. A field consisting of several sources can be assembled in post-processing using the solutions obtained for each one individually. While the standard units for the output matrix are Pascal, the KRAKEN plotting routines work with Transmission Loss (TL) between two points. Representing these by the pressures p_0 and p_1, TL is defined as

$$TL(p_1) = -20log_{10}(\frac{p_1}{p_0})\,. \tag{9}$$

4 BENCHMARKING

While KRAKEN has been conceived to handle complex interactions of sound between different media, something that is not captured by the traditional FW-H analogy, it does share the latter's limitations when it comes to range dependent environmental characteristics, such as bathymetry and the sound speed profile. However, several solutions can be glued together to yield a range-dependent noise field with KRAKEN. To determine how well this process is performed, some benchmark cases were run to compare the KRAKEN's results against BELLHOP. This ray-theory based model enjoys greater simplicity in its setup and can deal directly with variable media, but is limited to just one layer, resulting in solutions that neglect refraction and other interface effects.

In this section, two benchmark cases will be presented. The first highlights KRAKEN's handling of a variable sound speed profile, while the second illustrates how to ensure a proper treatment of an uneven sea-bottom.

4.1 Range-varying sound speed profile

A simple, flat and non-rigid floor, single source environment was set up, as described by Pregitzer[9]. The sound speed profile used was taken from the set of example files provided with the Acoustics Toolbox, and is illustrated in figure 1. The numerical mesh used to solve for the normal modes included approximately 12 points per wavelength, and results are projected onto a grid of 500 m horizontal and 100 m vertical spacing.

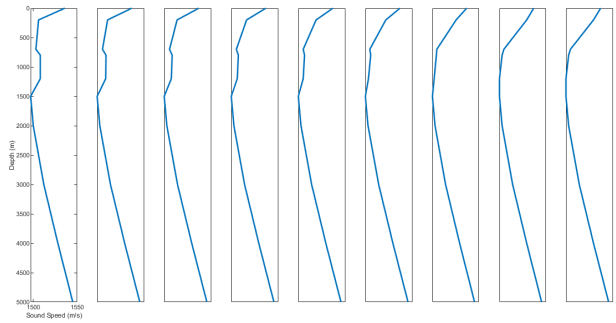

Figure 1: Sound speed profiles for each range segment considered in the range-dependent test case. Each segment is 12.5 km long.

Since KRAKEN solves only segments of constant characteristics, a choice must be made regarding the matching conditions used to glue together the different segments. Figures 2(b)-(c) show the transmission loss for two different options. The latter includes terms relating to the coupling of depth and range modes of propagation, which is more realistic but results in increased run-times. The so called adiabatic option neglects these terms, and is also illustrated in the Figure 2.

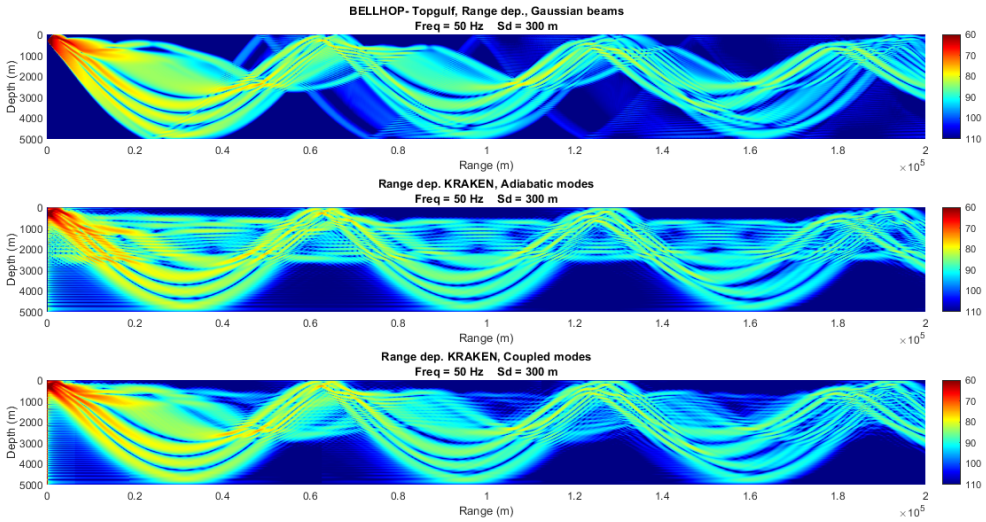

Figure 2: Transmission Loss (dB) plots over range and depth of the range-dependent test case run with (a)BELLHOP, (b)KRAKEN adiabatic modes, and (c)KRAKEN coupled modes.

The differences between BELLHOP, adiabatic KRAKEN and coupled KRAKEN are directly observable. Both KRAKEN cases show a propagation of earlier perturbations which the algorithm has difficulty in dissipating. The coupled mode approach allows the channel created by the dent in the sound speed profile illustrated in figure 1 to be dissipated as the dent gets smoothed out. However, when neglecting the coupling terms, the imposed matching conditions ensure perturbations are propagated over much longer distances. On the other hand, the transmission loss values are so high at this stage, that in practice background environmental noise would be of a much higher order of magnitude than these differences.

4.2 Wedge-shaped bathymetry

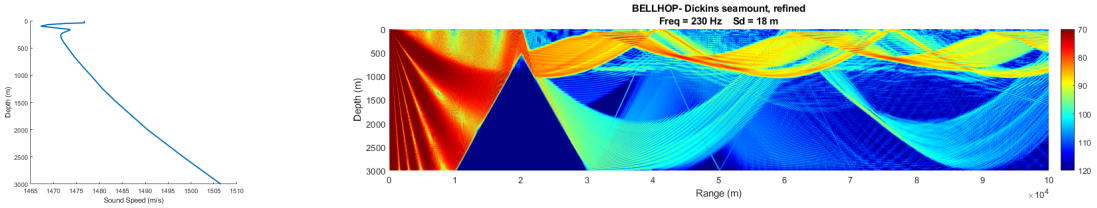

Figure 3: (a)Sound speed profile, and (b) Transmission Loss (dB) plot over range and depth for the wedge-shaped floor case using BELLHOP.

The same basic environment as previously described was modified to include a triangular hill on the ocean floor, with a slope of 14.5°on either side. The sound speed profile was maintained constant throughout, and is illustrated in figure 3(a), adapted once again from data provided by the Acoustics Toolbox. A transmission loss plot for the BELLHOP run is presented in figure 3(b). Given KRAKEN's ability to consider layers of different media, unlike BELLHOP, again two cases were run to determine the best approach when modelling sediment at the ocean floor. The first case, shown in figure 4(a), sets the bottom boundary at a constant depth of 3000 metres, modelling the hill through a second acoustic medium. The alternative approach, as seen in figure 4(b), uses just one medium and changes

the bottom boundary of each segment according to the local slope of the hill.

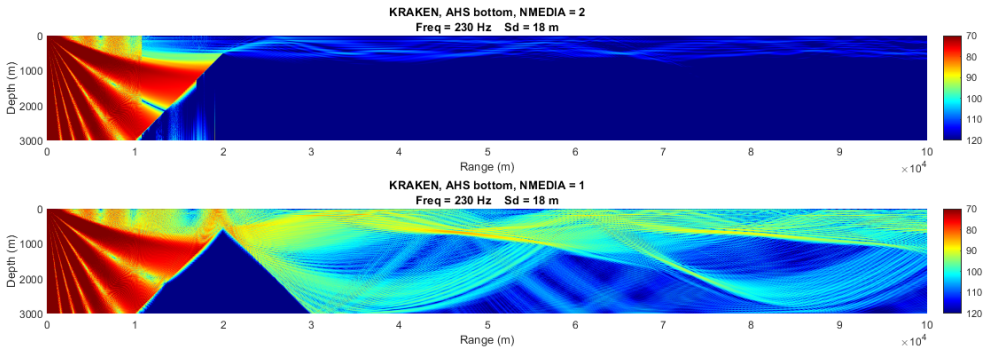

Figure 4: Transmission Loss (dB) plots over range and depth for the varying bathymetry, range-dependent case run with KRAKEN for (a)wedge as a second medium, and (b)wedge as part of the acousto-elastic halfspace-like bottom boundary condition

On the left-hand side of the slope, all three runs show essentially the same behaviour, with reflection between the climbing bottom and the ocean surface clearly identifiable. On the descending side, however, notable differences exist between the two KRAKEN cases.

5 VERIFICATION

This section will provide an overview of the verification methods employed and a discussion of results. The setup of each problem is detailed by Pregitzer[9]. To conclude, a run-time analysis for various test cases will also be given.

5.1 Methodology

Numerical errors are made up of a round-off, an iterative, and a discretization error[16]. The first two are related to the finite precision offered by computers when storing values (double-precision in the case of KRAKEN) and the intrinsic non-linearity of the equations being solved, respectively. The third error is associated with the numerical discretization and the resulting mesh on which the computations are performed. This is the only aspect directly in control of the end-user, and the focus of this analysis.

In order to verify calculation convergence, total acoustic energy e_{ac}, as defined by equation (10), needs to be calculated, because its conservation across different numerical meshes is one of the main properties which can indicate whether or not a problem is well posed.

$$e_{ac} = \frac{|p|^2}{\rho c} \,. \tag{10}$$

If conservation is checked, local variable convergence can then be determined, which will give an indication of the numerical uncertainty associated with the local pressure, and hence sound level. For this purpose, average values are calculated at the centre of each cell whose nodes are made up of grid points.

Numerical uncertainty can be estimated by running the same case under different mesh sizes. For this purpose, the Numerical Uncertainty Analysis (NUA) program[17] is used. This tool is able to determine the relationship between obtained results and successively finer mesh sizes, allowing the order of convergence to be studied and ideal meshes to be selected.

5.2 Comparison of methods

Verification was first studied for a simple, flat-bathymetry case, with a typical sound speed profile[18] using KRAKENC. The source is placed at the origin, with frequencies ranging from 60 to 400 Hz, and numerical meshes containing 12-70 points per wavelength. The environment and the three points to be studied are illustrated in figure 5.

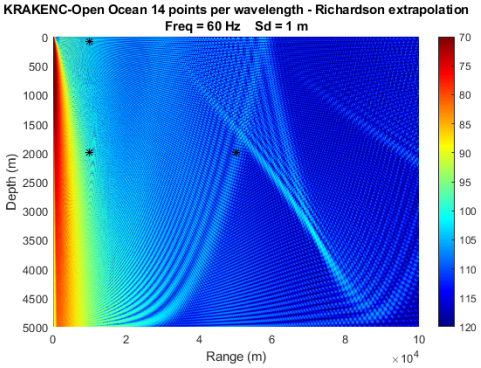

Figure 5: Transmission Loss (dB) plot for the 60 Hz case with a mesh size of 14 points per wavelength.

First, pressure convergence was studied, with local values exhibiting good behaviour and very low uncertainty levels for low frequencies as shown in figure 6(a). However, for higher frequencies, some points started exhibiting more complex behaviour, as in figures 6(b) and (c). These results illustrate the need to calculate acoustic energy and its convergence, in order to compensate for local fluctuations at individual points. Upon calculation of the total acoustic energy following the previously described methodology, all frequencies exhibited the same behaviour, as shown in figure 7, confirming convergence and low numerical uncertainty.

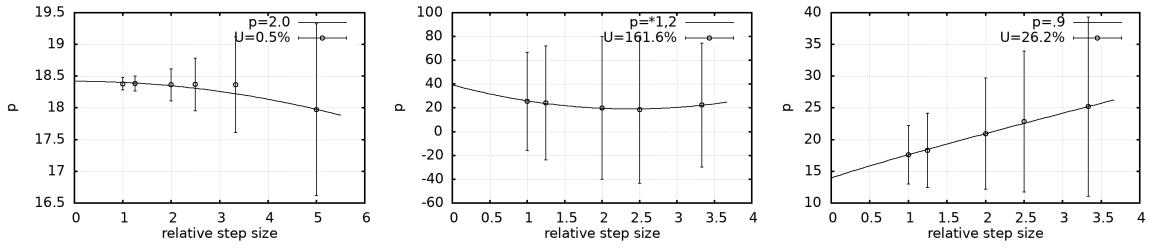

6

Figure 6: Numerical uncertainty study related to the amplified relative pressure for a frequency of (a)60 Hz, (b)200 Hz at the bottom left point, and (c)400 Hz at the bottom right point.

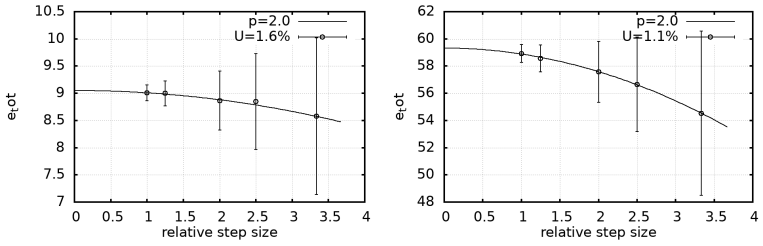

Figure 7: Numerical uncertainty pertaining to the total acoustic energy for various meshes, run at (a)200 Hz and(b)400 Hz.

5.3 Run-time analysis

By running several simple test cases, it was possible to study the relationship between run-time and various environment properties, such as number of modes, frequency and mesh size. Figure 8(a) shows the linear relationship between the number of modes in the problem and its frequency.

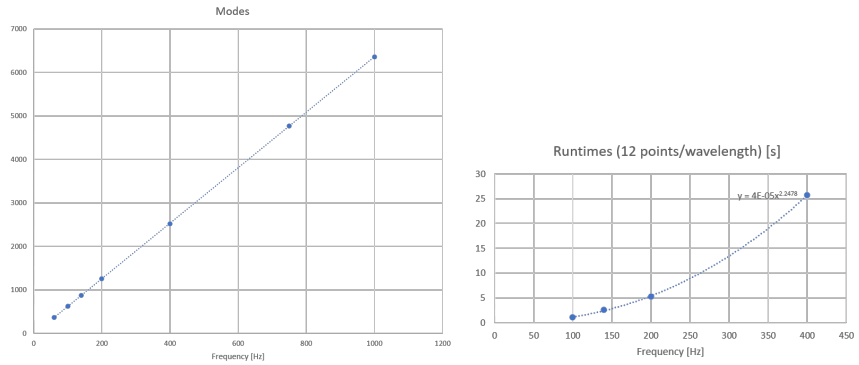

Figure 8: Relationship between (a)normal modes and frequency, and (b)run-time and points per wavelength.

A common parameter arising in KRAKEN is the number of points per wavelength because the program explicitly requires a numerical mesh resolution of at least 10 points per wavelength to run. As such, the mesh requirements will scale with frequency, and can be normalized and compared by using this parameter. Interestingly, when plotted against this value, the run-time data fit neatly in a quadratic equation, as evidenced in figure 8(b).

From this, result, one can conclude that significant computational expenses can be mitigated by assigning separate mesh sizes to different frequencies, while complying with the minimum resolution for all of them. For problems requiring the solution of various environments (any range-dependent problem), the run-times could be significantly reduced by parallelising the solvers for each one.

6 VALIDATION

6.1 Modelling the experiment

The computational domain is illustrated in figure 9(a). Measurement points were divided into two groups, called Transect-1 and Transect-2[5]. The first consists of four points following a downward slope, along a bearing of approximately 45°due north-west. The second set of points lies due north-east at a bearing of 60°, where the sea-floor depth remains approximately constant.

The first step in computing the pressure field due to the device is to discretize the horizontal domain into a number of triangles, by way of the Delaunay triangulation algorithm[19]. Figure 9(b) shows the resulting computational domain, along with the approximate directions of the transects.

Since no data were available on the characteristics of the sea-bottom at the device location in Peniche, estimates had to be obtained from documentation[20],[21]. Table 1 collects the used values.

Table 1: Estimated properties of the sandy bottom in the experiment surroundings. The quality factor Q is defined as $Q = \frac{\pi f}{\alpha c}$, where α is the attenuation.

c_p (m/s)	c_s (m/s)	ρ (kg/m^3)	Q_p	Q_s
1885	290	2.1	34	25

The chosen frequencies to be run were 125, 500 and 1600 Hz. The first two are the most relevant

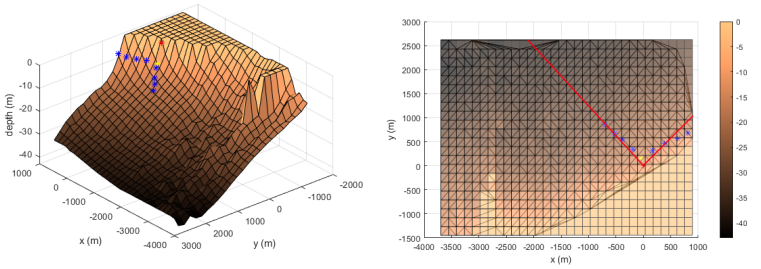

Figure 9: Bathymetric representation of the environment in (a)a three-dimensional perspective, and (b)a top-view illustrating the Delauney triangulation. Blue points represent the hydrophone coordinates, the red point is the source's location, and the yellow point is where noise emission was measured. The positive x- and y- axes point due East and North, respectively.

for the device, while the third one represents a higher frequency at which some of the normal mode model assumptions should work better. This is because, at depths of less than 30 m, the sea-floor is still very well inside the distance classified as near-field for low frequencies. At the regular water speed of sound of 1500 m/s, a sound wave emitted at 125 Hz has a wavelength of about 12 m. This may affect the nature of the eigenvalues to be found by KRAKEN and may lead to diverging solutions.

Finally, proper validation is only possible by verifying convergence of the obtained solution. As such, various mesh sizes, ranging from 12 to 80 points per wavelength, were used initially, and energy analysis followed that described in section 5.1.

Following this, a second analysis was run with fixed mesh sizes across all frequencies, ranging from 50 to 500 points per meter in depth, in an attempt to improve the obtained results. For this new case, the 2500 Hz frequency level, representing the upper limit of noise emission by the energy device, was also analysed.

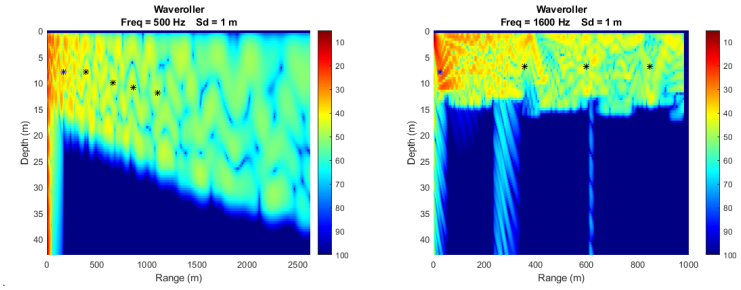

Figure 10: Cross-sectional TL plot with range and depth for the approximate (a)Transect-1 at 500 Hz, and (b)Transect-2 at 1600 Hz.

The test-case properties are summed up as: frequencies of 125 Hz, 500 Hz, 1600 Hz and 2500 Hz; vacuum used as the top boundary condition (BC); the bottom BC consists of an acousto-elastic halfspace as described in table 1; the mesh for the first run with 32-80 points per wavelength; mesh for second run with 50-500 points per wavelength; results presented on a uniform grid with spacing of $\Delta r = 1m$, $\Delta z = 0.5m$. Some qualitative solutions, along with the approximate locations of the measurement points, are presented in figures 10(a)-(b).

As previously discussed in section 5, acoustic energy is the variable for which uncertainty will be determined. However, given that this does not represent the same property as the experimentally measured Sound Pressure Level (SPL), an estimation of the numerical uncertainty relating to the Transmission Loss (TL) must be obtained, so that results can later be validated.

From equation (10), we can write that the converged value of the variable, e_{conv}, lies in the range of

$$e_{conv} = e_{comp}(1 \pm u_e) = \frac{[p\,(1 \pm u_p)]^2}{\rho\,(1 \mp u_\rho)\,c\,(1 \mp u_c)}\,, \tag{11}$$

where u_e and u_p are the numerical uncertainty associated with the acoustic energy and pressure, u_ρ and u_c are the measurement uncertainty related to density ρ and speed of sound c, respectively, and e_{comp} and p are computed values. From this equation, the upper and lower bounds for the numerical uncertainty associated with pressure can be found, which can then be used to calculate the upper and lower bounds of the Transmission Loss error as

$$\epsilon_{TL}^{\pm} = \mp 20 log_{10}\left(\sqrt{(1 \mp u_e)\,(1 \pm u_c)\,(1 \pm u_\rho)}\right)\,. \tag{12}$$

6.2 Baseline solution

For the 125 and 500 Hz cases, no consistent results were obtained. For the former frequency, KRAKEN failed to calculate any modes, while in the latter case no energy convergence was verified, with very erratic results for different mesh sizes. On the other hand, the 1600 Hz runs showed strong stability, with numerical uncertainty values below 3%, as exemplified in figure 11.

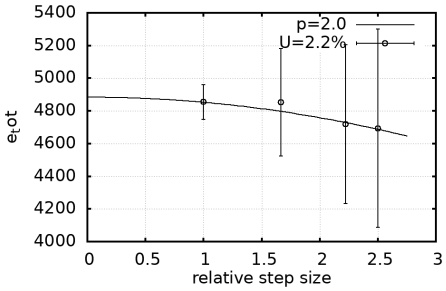

Figure 11: Total acoustic energy numerical uncertainty study for the approximate Transect-1 bearing at 1600 Hz. The value of the acoustic energy was amplified by several orders of magnitude to improve the calculation.

Even though the two most relevant frequency runs for the energy device model failed to yield proper results, data were still available for the 1600 Hz band. As such, a comparison to the measured experimental measurements is provided. Using equation (12) together with the NUA analysis to calculate the error of the computational results, and applying a standard deviation uncertainty to the experimental data, figures 12(a)-(b) were generated comparing both sets of results.

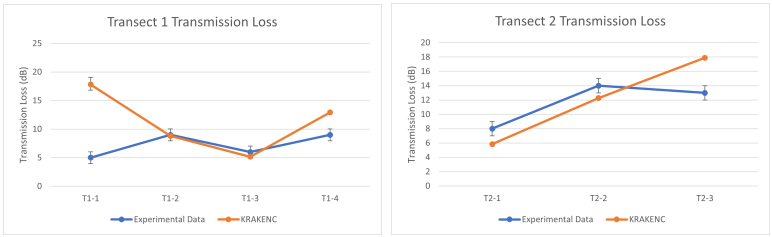

Figure 12: Transmission Loss data validation at 1600 Hz for Transects (a)1 and (b)2.

Except for T1-1, which shows higher Transmission Loss than would be expected, all other points match the measurements well. At the furthest points of each transect, values tend to diverge, but this is due to the non-existing background noise in KRAKEN.

6.3 Enhanced solution

During the elaboration of this work, erratic behaviour was identified to be caused when the numerical mesh does not contain all sound speed profile data given as input. As such, a new set of runs was computed in an attempt to fix the issues observed previously, possibly caused by the frequency scaling when automatically generating the meshes. However, as before, the 125 Hz case failed to yield any relevant modes, confirming that it is too low a frequency for these depths using the current methods. Near-field models, such as Green's function algorithms, are more appropriate for distances within 5 wavelengths, as is the case at this low frequency.

As for the higher frequency cases, the results are well-behaved and converging as expected. Consequently, the data can be compared to experimental results, and this is presented, for cases with relevant new behaviour, in figures 13(a)-(c).

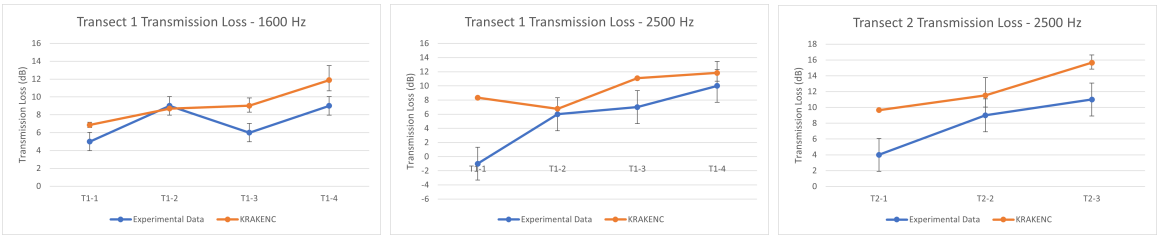

Figure 13: Enhanced run data validation for (a)Transect-1 at 1600 Hz, (b)Transect-1 at 2500 Hz, and (c)Transect-2 at 2500 Hz.

As in the previous section, the 1600 Hz case seems to be in good agreement with the experimental data, except for T1-3. For this point, Transmission Loss levels vary greatly with depth, and it is difficult to know exactly at what point the hydrophone was placed. Depending on this, the computational solution may agree with the measurement. At 2500 Hz, the solution agrees well for both transects but an unexpected measurement at T2-1, where a higher SPL was detected than at the source, makes it more difficult to draw comparisons for that point, once again possibly indicating that the estimated experimental uncertainty is too conservative.

The erratic behaviour observed was shown not to be due to mesh/sound speed profile mismatch, as it persisted in both sets of solutions. It is possible the usage of very small elements in the domain discretization is preventing the field calculation algorithm from properly matching different cells, seeing as the mode calculation itself seemed to be mostly well behaved at 500 Hz. As such, the problem seems to be manifesting when assembling the solution for the entire domain.

On the experimental side, the sampling of a single depth point makes it hard to directly compare measured and computed results, given their sensitivity to depth. Furthermore, the cyclical nature of the energy device noise generation is a problem for KRAKEN, which acts in the frequency domain and computes a stationary pressure field originating from a continuous sound source.

7 CONCLUSIONS

The normal mode KRAKENC algorithm has been shown to be an appropriate program for the calculation of noise fields in a varying, shallow environment. Its performance was concluded to be qualitatively equivalent to BELLHOP when no complex refraction effects are relevant. Furthermore, it was shown that local acoustic energy is a more resilient parameter to varying numerical mesh sizes.

At distances below about 5 wavelengths, a point source is no longer a valid model and as such difficulties at very shallow depths arose when validating KRAKENC calculations against experimental data. This has lead to successful validation of results for frequencies above 1000 Hz only. How-

ever, outside of these extreme conditions, results showed good agreement, and KRAKENC may be considered an appropriate algorithm applicable to noise analysis around energy devices near the coast.

To solve the encountered problems at lower frequencies, perhaps a finer mode sampling in depth or of larger areas for acoustic energy calculation may improve results; neglecting low bathymetry slopes and modelling the sea-floor as flat may also help; the coupling of KRAKEN computations with near-field solutions obtained from Green's function, parabolic, or F-WH algorithms may also yield better results for extreme cases, and is an area of interest for future research.

Finally, experimental measurements at more depth points would also help to better understand the correlation between computations and detected values in the field.

REFERENCES

[1] Thomas P. Lloyd, Stephen R. Turnock, and Victor F. Humphrey. Modelling techniques for underwater noise generated by tidal turbines in shallow waters. In 30^{th} *International Conference on Ocean, Offshore and Arctic Engineering*, Rotterdam, The Netherlands, June 2011. University of Southampton. OMAE2011-49994.

[2] J. E. Ffowcs Williams and D. L. Hawkings. Sound generation by turbulence and surfaces in arbitrary motion. *Philosophical Transactions of the Royal Society A: Mathematical, Physical and Engineering Sciences*, 264(1151):321–342, 1969.

[3] G. Vaz, F. Jaouen, and M. Hoekstra. Free-surface viscous flow computations. validation of urans code refresco. In *ASME 28th International Conference OMAE2009*, Honolulu, Hawaii, June 2009.

[4] Michael B. Porter. The kraken normal mode progrm (draft). May 2001.

[5] Erica Cruz, Teresa Simas, and Erkki Kasanen. Discussion of the effects of the underwater noise radiated by a wave energy device - portugal. In 11^{th} *European Wave and Tidal Energy Conference*, Nantes, France, September 2015. WavEC Offshore Renewables.

[6] Michael B. Porter and Edward L. Reiss. A numerical method for ocean-acoustic normal modes. *The Journal of the Acoustical Society of America*, 76(1), July 1984.

[7] https://oalib-acoustics.org/ accessed on April 21st 2020.

[8] Michael B. Porter. The bellhop manual and user's guide: Preliminary draft. January 2011.

[9] Pedro Pregitzer. Underwater acoustic impact of marine renewable energy devices: Modelling approaches. Master's thesis, Instituto Superior Técnico, January 2021.

[10] Allan D. Pierce. *Acoustics: an introduction to its physical principles and applications*. Springer, 3^{rd} edition, 2019. ISBN 9783030112141.

[11] Finn B. Jensen, William A. Kuperman, Michael B. Porter, and Henrik Schmidt. *Computational Ocean Acoustics*. Springer, 2^{nd} edition, 2011.

[12] Vladimir A. Marchenko. *Sturm-Liouville Operators and Applications*. Birkhäuser Basel, 1986.

[13] Joel H. Ferziger and Milovan Perić. *Computational Methods for Fluid Dynamics*. Springer, 3^{rd}, rev. edition, 2002. ISBN 978-3-642-56026-2.

[14] D.C. Stickler. Normal-mode program with both the discrete and branch line contributions. *The Journal of the Acoustical Society of America*, 57:856–861, 1970.

[15] J.H. Wilkinson. *The Algebraic Eigenvalue Problem*. Oxford University Press, 1965.

[16] L. Eça and M. Hoekstra. Evaluation of numerical error estimation based on grid refinement studies with the method of the manufactured solutions. *Computers and Fluids*, 38:1580–1591, 2009.

[17] L. Eça and M. Hoekstra. A procedure for the estimation of the numerical uncertainty of cfd calculations based on grid refinement studies. *Journal of Computational Physics*, 262:104–130, 2014.

[18] https://staff.washington.edu/dushaw/WOA/ accessed on September 21st 2020.

[19] Charles Hirsch. *Numerical Computation of Internal and External Flows*. Butterworth-Heinemann, 2^{nd} edition, 2007.

[20] J. L. Wilson. *Carbonate Seismology*, chapter 2. Number 6 in Geophysical Developments Series. Society of Exploration Geophysicists, 1997. ISBN 9781560800385.

[21] Rolf Sidler and Klaus Holliger. Seismic reflectivity of the sediment-covered seafloor: effects of velocity gradients and fine-scale layering. *Geophysical Journal International*, 181:521–531, 2010.